

# Diffusion Equations for Medical Images

Moo K. Chung

University of Wisconsin-Madison, USA

[mkchung@wisc.edu](mailto:mkchung@wisc.edu)

In brain imaging, the image acquisition and processing processes themselves are likely to introduce noise to the images. It is therefore imperative to reduce the noise while preserving the geometric details of the anatomical structures for various applications. Traditionally Gaussian kernel smoothing has been often used in brain image processing and analysis. However, the direct application of Gaussian kernel smoothing tend to cause various numerical issues in irregular domains with boundaries. For example, if one uses large bandwidth in kernel smoothing in a cortical bounded region, the smoothing will blur signals across boundaries. So in kernel smoothing and regression literature, various ad-hoc procedures were introduced to remedy the boundary effect.

Motivated by Perona & Malik (1990), diffusion equations have been widely used in brain imaging as a form of noise reduction. The most natural straightforward way to smooth images in irregular domains with boundaries is to formulate the problem as boundary value problems using partial differential equations. Numerous diffusion-based techniques have been developed in image processing (Sochen et al. 1998, Malladi & Ravve 2002, Tang et al. 1999, Taubin 2000, Andrade et al. 2001, Chung et al. 2001, Chung, Worsley, Robbins, Paus, Taylor, Giedd, Rapoport & Evans 2003, Chung, Robbins & Evans 2005, Chung & Taylor 2004, Cachia, Mangin, Rivière, Papadopoulos-Orfanos, Kherif, Bloch & Régis 2003, Cachia, Mangin, Rivière, Kherif, Boddaert, Andrade, Papadopoulos-Orfanos, Poline, Bloch, Zilbovicius, Sonigo, Brunelle & Régis 2003, Joshi et al. 2009). In this paper, we will overview the basics of isotropic diffusion equations and explain how to solve them on regular grids and irregular grids such as graphs.

## 1 Diffusion as a Cauchy problem

Consider  $\mathcal{M} \in \mathbb{R}^d$  to be a compact differentiable manifold. Let  $L^2(\mathcal{M})$  be the space of square integrable functions in  $\mathcal{M}$  with inner product

$$\langle g_1, g_2 \rangle = \int_{\mathcal{M}} g_1(p)g_2(p) d\mu(p), \quad (1)$$

where  $\mu$  is the Lebesgue measure such that  $\mu(\mathcal{M})$  is the total volume of  $\mathcal{M}$ . The norm  $\|\cdot\|$  is defined as

$$\|g\| = \langle g, g \rangle^{1/2}.$$

The linear partial differential operator  $\mathcal{L}$  is *self-adjoint* if

$$\langle g_1, \mathcal{L}g_2 \rangle = \langle \mathcal{L}g_1, g_2 \rangle$$

for all  $g_1, g_2 \in L^2(\mathcal{M})$ . Then the eigenvalues  $\lambda_j$  and eigenfunctions  $\psi_j$  of the operator  $\mathcal{L}$  are obtained by solving

$$\mathcal{L}\psi_j = \lambda_j\psi_j. \quad (2)$$

Often (2) is written as

$$\mathcal{L}\psi_j = -\lambda_j\psi_j$$

so care should be taken in assigning the sign of eigenvalues.

**Theorem 1.** *The eigenfunctions  $\psi_j$  are orthonormal.*

*Proof.* Note  $\langle \psi_i, \mathcal{L}\psi_j \rangle = \lambda_j \langle \psi_i, \psi_j \rangle$ . On the other hand,  $\langle \mathcal{L}\psi_i, \psi_j \rangle = \lambda_i \langle \psi_i, \psi_j \rangle$ . Thus

$$(\lambda_i - \lambda_j) \langle \psi_i, \psi_j \rangle = 0.$$

For any  $\lambda_i \neq \lambda_j$ ,  $\langle \psi_i, \psi_j \rangle = 0$ , orthogonal. For  $\psi_j$  to be orthonormal, we need  $\langle \psi_j, \psi_j \rangle = 1$ . This is simply done by absorbing the constant multiple into  $\psi_j$ . Thus,  $\{\psi_j\}$  is orthonormal.  $\square$

In fact  $\psi_j$  is the basis in  $L^2(\mathcal{M})$ . Consider 1D eigenfunction problem

$$\frac{\partial^2}{\partial x^2} \psi_j(x) = -\lambda_j \psi_j(x)$$

in interval  $[-l, l]$ . We can easily check that

$$\psi_{1j} = \cos\left(\frac{j\pi x}{l}\right), \quad \psi_{2j} = \sin\left(\frac{j\pi x}{l}\right), \quad j = 1, 2, \dots$$

are eigenfunctions corresponding to eigenvalue  $\lambda_j = \left(\frac{j\pi}{l}\right)^2$ . Also  $\psi_{10} = 1$  is trivial first eigenfunction corresponding to  $\lambda_0 = 0$ . The multiplicity of eigenfunctions is caused by the symmetric of interval  $[-l, l]$ . Based on trigonometric formula, we can show that the eigenfunctions are orthogonal.

$$\begin{aligned} \int_{-l}^l \psi_{1i}(x)\psi_{1j}(x) dx &= 0 \text{ if } i \neq j \\ \int_{-l}^l \psi_{2i}(x)\psi_{2j}(x) dx &= 0 \text{ if } i \neq j \\ \int_{-l}^l \psi_{1i}(x)\psi_{2j}(x) dx &= 0 \text{ for any } i, j \end{aligned}$$

From  $\psi_{1j}^2(x) + \psi_{2j}^2(x) = 1$  and due to symmetry

$$\int_{-l}^l \psi_{1j}^2(x) dx = \int_{-l}^l \psi_{2j}^2(x) dx = l.$$

Thus

$$\begin{aligned}\psi_{10} &= \frac{1}{\sqrt{2l}}, \\ \psi_{1j} &= \frac{1}{\sqrt{l}} \cos\left(\frac{j\pi x}{l}\right), \\ \psi_{2j} &= \frac{1}{\sqrt{l}} \sin\left(\frac{j\pi x}{l}\right), \quad j = 1, 2, \dots\end{aligned}$$

are orthonormal basis in  $[-l, l]$ .

Consider a Cauchy problem of the following form:

$$\frac{\partial g}{\partial t}(p, t) + \mathcal{L}g(p, t) = 0, g(p, t = 0) = f(p), \quad (3)$$

where  $t$  is time variable and  $p$  is spatial variable.

The initial functional data  $f(p)$  can be further stochastically modeled as

$$f(p) = \nu(p) + \epsilon(p), \quad (4)$$

where  $\epsilon$  is a stochastic noise modeled as a zero-mean Gaussian random field, i.e.,  $\mathbb{E}\epsilon(p) = 0$  at each point  $p$  and  $\nu$  is the unknown signal to be estimated. PDE (3) diffuses noisy initial data  $f$  over time and estimate the unknown signal  $\nu$  as a solution. Diffusion time  $t$  controls the amount of smoothing and will be termed as the *bandwidth*. The unique solution to equation (3) is given as follows. This is a heuristic proof and more rigorous proof is given later.

**Theorem 2.** *For the self-adjoint linear differential operator  $\mathcal{L}$ , the unique solution of the Cauchy problem*

$$\frac{\partial g}{\partial t}(p, t) + \mathcal{L}g(p, t) = 0, g(p, t = 0) = f(p) \quad (5)$$

is given by

$$g(p, t) = \sum_{j=0}^{\infty} e^{-\lambda_j t} \langle f, \psi_j \rangle \psi_j(p). \quad (6)$$

*Proof.* For each fixed  $t$ , since  $g \in L^2(\mathcal{M})$ ,  $g$  has expansion

$$g(p, t) = \sum_{j=0}^{\infty} c_j(t) \psi_j(p). \quad (7)$$

Substitute equation (7) into (5). Then we obtain

$$\frac{\partial}{\partial t} c_j(t) + \lambda_j c_j(t) = 0 \quad (8)$$

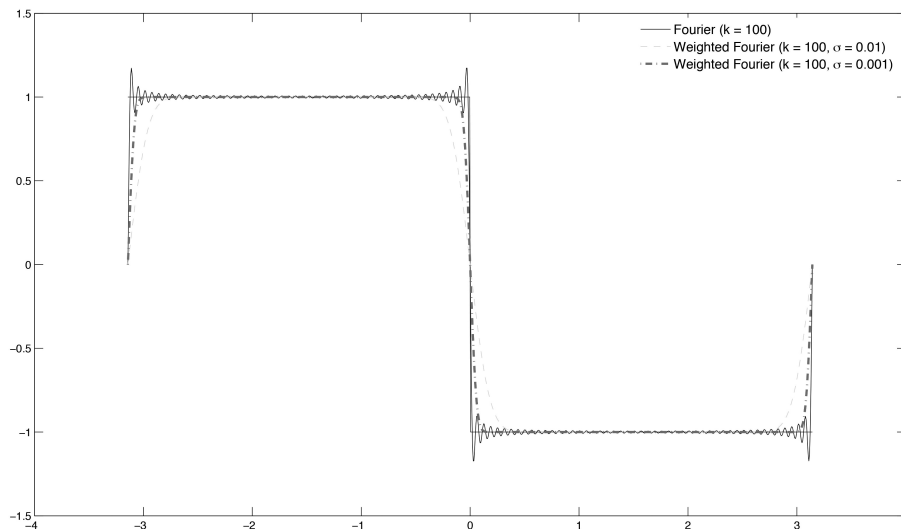


Fig. 1: Reduction of Gibbs phenomenon in weighted Fourier series (WFS). The figure was generated by Yuan Wang of University of South Carolina (Wang et al. 2018).

for all  $j$ . The solution of equation (8) is given by

$$c_j(t) = b_j e^{-\lambda_j t}.$$

So we have solution

$$g(p, t) = \sum_{j=0}^{\infty} b_j e^{-\lambda_j t} \psi_j(p).$$

At  $t = 0$ , we have

$$g(p, 0) = \sum_{j=0}^{\infty} b_j \psi_j(p) = f(p).$$

The coefficients  $b_j$  must be the Fourier coefficients  $\langle f, \psi_j \rangle$  and they are uniquely determined.  $\square$

The implication of Theorem 2 is obvious. The solution decreases exponentially as time  $t$  increases and smoothes out high spatial frequency noise much faster than low frequency noise. This is the basis of many of PDE-based image smoothing methods. PDE involving self-adjoint linear partial differential operators such as the Laplace-Beltrami operator or iterated Laplacian have been widely used in medical image analysis as a way to smooth either scalar or vector data along anatomical boundaries (Andrade et al. 2001, Bulow 2004, Chung, Worsley, Robbins, Paus, Taylor, Giedd, Rapoport & Evans 2003). These methods directly solve PDE using standard numerical techniques such as the finite

difference method (FDM) or the finite element method (FEM). The main shortcoming of solving PDE using FDM or FEM is the numerical instability and the complexity of setting up the numerical scheme. The analytic approach called weighted Fourier series (WFS) differs from these previous methods in such a way that we only need to estimate the Fourier coefficients in a hierarchical fashion to solve PDE (Chung et al. 2007).

*Example 1.* Consider 1D differential operator  $\mathcal{L} = \frac{\partial^2}{\partial x^2}$ . The corresponding Cauchy problem is 1D diffusion equation

$$\frac{\partial g}{\partial t}(p, t) + \frac{\partial^2 g}{\partial x^2}(p, t) = 0, g(p, t = 0) = f(p), p \in [-l, l].$$

Then the solution of this problem is given by Theorem 2:

$$g(p, t) = a_0 \psi_{10} + \sum_{j=1}^{\infty} a_j e^{-\lambda_j t} \psi_{1j}(p) + b_j e^{-\lambda_j t} \psi_{2j}(p),$$

where

$$\begin{aligned} a_0 &= \frac{1}{\sqrt{2l}} \int_{-l}^l f(p) dp, \\ a_j &= \frac{1}{\sqrt{l}} \int_{-l}^l f(p) \cos\left(\frac{j\pi x}{l}\right) dp, \\ b_j &= \frac{1}{\sqrt{l}} \int_{-l}^l f(p) \sin\left(\frac{j\pi x}{l}\right) dp \end{aligned}$$

for  $j = 1, 2, \dots$ .

## 2 Finite difference method

One way of solving diffusion equations numerically is to use finite differences. We will discuss how to differentiate images. There are numerous techniques for differentiation proposed in literature. We start with simple example of image differentiation in 2D image slices. Consider image intensity  $f(x, y)$  defined on a regular grid, i.e.,  $(x, y) \in \mathbb{Z}^2$ . Assume the pixel size is  $\delta x$  and  $\delta y$  in  $x$ - and  $y$ -directions. The partial derivative along the  $x$ -direction of image  $f$  is approximated by the finite difference:

$$\frac{\partial f}{\partial x}(x, y) = \frac{f(x + \delta x, y) - f(x, y)}{\delta x}.$$

The partial derivative along the  $y$ -direction of image  $f$  is approximated similarly.  $\frac{\partial f}{\partial x}(x, y)$  and  $\frac{\partial f}{\partial y}(x, y)$  are called the *first order derivatives*. Then the *second order derivatives* are defined by taking the finite difference twice:

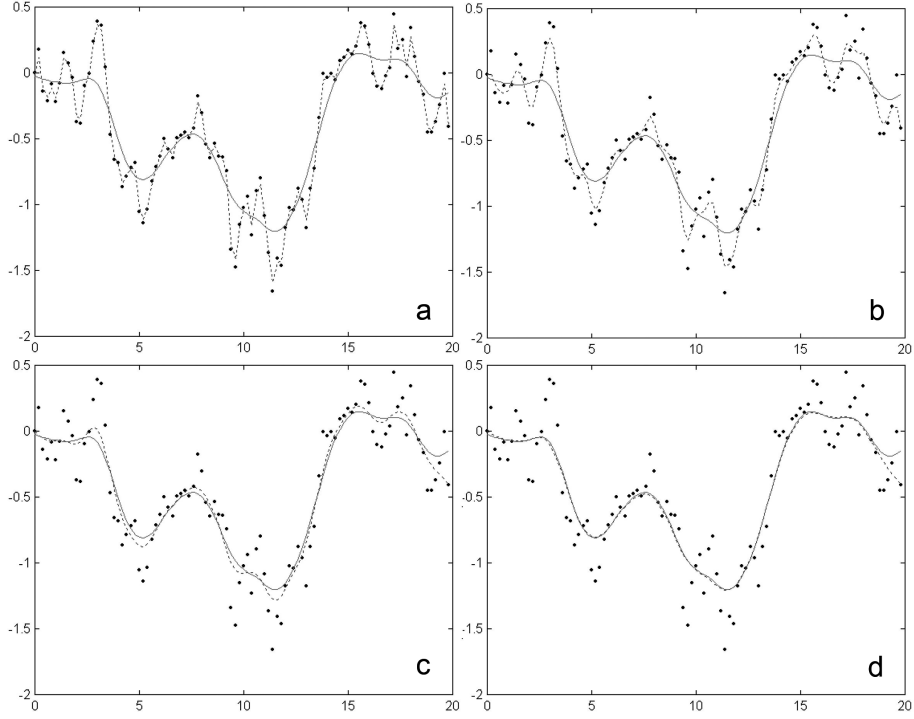


Fig. 2: Gaussian kernel smoothing (solid line) and diffusion smoothing (dotted line). (a) before diffusion (b) after 0.05 seconds (5 iterations) (c) after 0.25 seconds (25 iterations) (d) after 0.5 seconds (50 iterations).

$$\begin{aligned}\frac{\partial^2 f}{\partial x^2}(x, y) &= \left[ \frac{f(x + \delta x, y) - f(x, y)}{\delta x} - \frac{f(x, y) - f(x - \delta x, y)}{\delta x} \right] / \delta x \\ &= \frac{f(x + \delta x, y) - 2f(x, y) + f(x - \delta x, y)}{\delta x^2}\end{aligned}$$

Similarly, we also have

$$\frac{\partial^2 f}{\partial y^2}(x, y) = \frac{f(x, y + \delta y) - 2f(x, y) + f(x, y - \delta y)}{\delta y^2}.$$

Other partial derivatives such as  $\frac{\partial^2 f}{\partial x \partial y}$  are computed similarly.

## 2.1 1D diffusion by finite difference

Let us implement 1D version of diffusion equations (Figure 2). Suppose we have a smooth function  $f(x, t)$  which is a function of position  $x \in \mathbb{R}$  and time  $t \in \mathbb{R}^+$ .

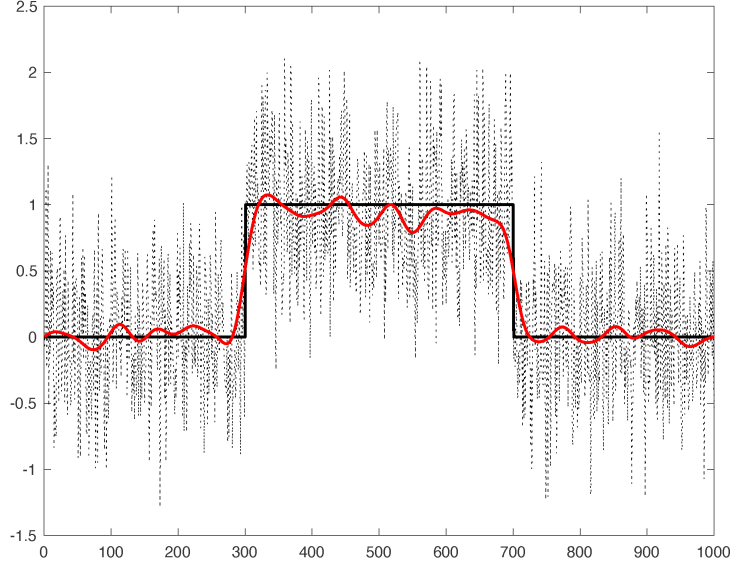


Fig. 3: Diffusion of simulated data (dotted line) and the ground truth (black line). The both methods using `conv.m` and `toeplitz.m` all converge to the red line.

1D isotropic heat equation is then defined as

$$\frac{\partial f}{\partial t} = \frac{d^2 f}{dx^2} \quad (9)$$

with initial condition  $f(x, t = 0) = g(x)$ . Differential equation (9) is then discretized as

$$f(x, t + \delta t) = f(x, t) + \delta t \frac{d^2 f}{dx^2}(x, y). \quad (10)$$

With  $t_k = k\delta t$  and starting from  $t = 0$ , (10) can be written as

$$f(x, t_{k+1}) = f(x, t_k) + \delta t \frac{f(x + \delta x, t_k) - 2f(x, t_k) + f(x - \delta x, t_k)}{\delta x^2}. \quad (11)$$

The above finite difference gives the solution at time  $t_{k+1}$ . To obtain the solution at any time, it is necessary to keep iterating many times with very small  $\delta t$ . If  $\delta t$  is too small, the computation is slow. If it is too large, the finite difference will diverge. Then the problem is finding the largest  $\delta t$  that grantee the convergence.

Numerically (11) is solved in MATLAB follows. We start with generating a step function as the ground truth (black line in Figure 3). We then add  $N(0, 0.5^2)$  noise.

```

x=1:1000;
noise=normrnd(0, 0.5, 1,1000);
signal= [zeros(1,300) ones(1,400) zeros(1,300)];
figure; plot(signal, 'k', 'LineWidth',2);
y= signal + noise;
hold on; plot(y, ':k');

```

The 2nd order finite difference is coded as  $L=[1 \ -2 \ 1]$ . Then it is convoluted with 3 consecutive data at a time in the code blow.

```

L = [1 -2 1]
g=y;
for i=1:10000
    Lg = conv(g,L,'same');
    g = g+ 0.01*Lg;
end
hold on;plot(g, 'b', 'LineWidth', 2);

```

Since the Laplacian is a linear operator, the above convolution can be written as the matrix multiplication. Any linear operation can be discretely encoded as matrix multiplication. Here the Laplacian is encoded using a Toeplitz matrix:

```

c=zeros(1,1000);
c(1:2)=[-2 1];
r=zeros(1,1000);
r(1:2)=[-2 1];
L = toeplitz(c,r);

```

The first 5 columns and rows of the Toeplitz matrix L is given by

```

L(1:5,1:5)
ans =
    -2     1     0     0     0
     1    -2     1     0     0
     0     1    -2     1     0
     0     0     1    -2     1
     0     0     0     1    -2

```

The diffusion is solved by sequential summation of matrix multiplications

```

g=y';
for i=1:10000
    g = g+ 0.01*L*g;
end
hold on;plot(g, 'g', 'LineWidth', 2);

```

The first and last rows of the the Toeplitz matrix L is  $[-2 \ 1 \ 0]$  and  $[0 \ 1 \ -2]$ , which is different from the 2nd order finite difference  $[1 \ -2 \ 1]$ . It will not matter since that may be viewed as the discrete Laplacian in the boundary. The

matrix form of Laplacian can be used in conjunction with the recently developed polynomial approximation method for solving heat diffusion on manifolds (Huang et al. 2020).

*Discrete maximum principle.* Since the diffusion smoothing and kernel smoothing are equivalent, The diffused signal  $f(x, t_{k+1})$  must be bounded by the minimum and the maximum of signal (Chung, Worsley, Robbins & Evans 2003). Let  $x_{i-1}, x_i, x_{i+1}$  be some points with gap  $\delta x$ .

$$\begin{aligned} f(x_i, t_{k+1}) &= f(x_i, t_k) + \delta t \frac{d^2 f}{dx^2}(x_i, t_k) \\ &\leq \max [f(x_{i-1}, t_k), f(x_i, t_k), f(x_{i+1}, t_k)]. \end{aligned}$$

Similarly, we can bound it below. Thus, the time step should be bounded by

$$\delta t \leq \max \left[ \left| \frac{f(x_{i-1}, t_j) - f(x_i, t_j)}{\frac{d^2 f}{dx^2}} \right|, \left| \frac{f(x_{i+1}, t_j) - f(x_i, t_j)}{\frac{d^2 f}{dx^2}} \right| \right].$$

## 2.2 Diffusion in $n$ -dimensional grid

In 2D, let  $(x_i, y_i)$  be pixels around  $(x, y)$  including  $(x, y)$  itself. Then using the 4-neighbor scheme, Laplacian of  $f(x, y)$  can be written as

$$\Delta f(x, y) = \sum_{i,j} w_{ij} f(x_i, y_i),$$

where the Laplacian matrix is given by

$$(w_{ij}) = \begin{pmatrix} 0 & 1 & 0 \\ 1 & -4 & 1 \\ 0 & 1 & 0 \end{pmatrix}.$$

Note that  $\sum_{ij} w_{ij} = 1$ .

Extending it further, consider  $n$ D. Let  $x = (x_1, x_2, \dots, x_n)$  be the coordinates in  $\mathbb{R}^n$ . Laplacian  $\Delta$  in  $\mathbb{R}^n$  is defined as

$$\Delta f = \frac{\partial^2 f}{\partial x_1^2} + \dots + \frac{\partial^2 f}{\partial x_n^2}.$$

Assume we have a  $n$ -dimensional hyper-cube grid of size is 1. Then we have

$$\begin{aligned} \Delta f(x) &= f(x_1 \pm 1, \dots, x_n) + \dots + f(x_1, \dots, x_n \pm 1) \\ &\quad - 2nf(x, y). \end{aligned}$$

This uses  $2n$  closest neighbors of voxel  $x$  to approximate the Laplacian.

It is also possible to incorporate  $2^n$  corners  $(x_1 \pm 1, \dots, x_n \pm 1)$  along with the  $2n$  closest neighbors for a better approximation of the Laplacian. In particular

in 2D, we can obtain a more accurate finite difference formula for 8-neighbor Laplacian:

$$(w_{ij}) = \frac{1}{9} \begin{pmatrix} 1 & 1 & 1 \\ 1 & -8 & 1 \\ 1 & 1 & 1 \end{pmatrix}.$$

Based on the estimation Laplacian on discrete grid, diffusion equation

$$\frac{\partial f}{\partial t} = \Delta f$$

is discretized as

$$f(x, t_{k+1}) = f(x, t_k) + \delta t \sum_{i,j} w_{ij} f(x_i, y_i). \quad (12)$$

with  $t_k = k\delta t$  and starting from  $t_1 = 0$ . From (12), we can see that the diffusion equation is solved by iteratively applying convolution with weights  $w_{ij}$ . In fact, it can be shown that the solution of diffusion is given by kernel smoothing.

### 3 Laplacian on planner graphs

In a previous section, we showed how to estimate the Laplacian in a regular grid. Now we show how to estimate Laplacian in irregular grid such as graphs and polygonal surfaces in  $\mathbb{R}^2$ . The question is how one estimate Laplacian or any other differential operators on a graph. Assume we have observations  $Y_i$  at each point  $p_i$ , which is assumed to follow additive model

$$Y_i = \mu(p_i) + \epsilon(p_i), \quad p_i \in \mathbb{R}^2$$

where  $\mu$  is a smooth continuous function and  $\epsilon$  is a zero mean Gaussian random field. We want to estimate at some node  $p_i$  on a graph:

$$\Delta\mu(p_0) = \frac{\partial^2 \mu}{\partial x^2} \Big|_{p_0} + \frac{\partial^2 \mu}{\partial y^2} \Big|_{p_0}.$$

Unfortunately, the geometry of the graph forbid direct application of finite difference scheme. To answer this problem, one requires the finite element method (FEM) (Chung 2001). However, we can use a more elementary technique called *polynomial regression*.

Let  $p_i = (x_i, y_i)$  be the coordinates of the vertices of the graph or polygonal surface. Let  $p_i$  be the neighboring vertices of  $p_0$ . We estimate the Laplacian at  $p_0$  by fitting a quadratic polynomial of the form

$$\mu(u, v) = \beta_0 + \beta_1 u + \beta_2 v + \beta_3 u^2 + \beta_4 uv + \beta_5 v^2. \quad (13)$$

We are basically assuming the unknown signal  $\mu$  to be the quadratic form (13). Then the parameters  $\beta_i$  are estimated by solving the normal equation:

$$Y_i = \beta_0 + \beta_1 x_i + \beta_2 y_i + \beta_3 x_i^2 + \beta_4 x_i y_i + \beta_5 y_i^2 \quad (14)$$

for all  $p_i$  that is neighboring  $p_0$ . For simplicity, we may assume  $p_0$  is translated to the origin, i.e.,  $x_0 = 0, y_0 = 0$ .

Let  $Y = (Y_1, \dots, Y_m)^\top$ ,  $\beta = (\beta_0, \dots, \beta_5)^\top$  and design matrix

$$\mathbb{X} = \begin{pmatrix} 1 & x_1 & y_1 & x_1^2 & x_1 y_1 & y_1^2 \\ 1 & x_2 & y_2 & x_2^2 & x_2 y_2 & y_2^2 \\ \dots & \dots & \dots & \dots & \dots & \dots \\ 1 & x_m & y_m & x_m^2 & x_m y_m & y_m^2 \end{pmatrix}.$$

Then we have the following matrix equation

$$Y = \mathbb{X}\beta.$$

The unknown coefficients vector  $\beta$  is estimated by the usual least-squares method:

$$\hat{\beta} = (\hat{\beta}_0, \dots, \hat{\beta}_5)^\top = (\mathbb{X}^\top \mathbb{X})^{-} \mathbb{X}^\top Y,$$

where  $^{-}$  denotes generalized inverse, which can be obtained through the singular value decomposition (SVD). Note that  $\mathbb{X}^\top \mathbb{X}$  is nonsingular if  $m < 6$ . In Matlab, `pinv` can be used to compute the generalized inverse, which is often called the *pseudo inverse*.

The generalized inverse often used is that of Moore-Penrose. It is usually defined as matrix  $\mathbb{X}$  satisfying four conditions

$$\mathbb{X}\mathbb{X}^{-}\mathbb{X} = \mathbb{X}, \quad \mathbb{X}^{-}\mathbb{X}\mathbb{X}^{-} = \mathbb{X}^{-},$$

$$(\mathbb{X}\mathbb{X}^{-})^\top = \mathbb{X}\mathbb{X}^{-}, \quad (\mathbb{X}^{-}\mathbb{X})^\top = \mathbb{X}^{-}\mathbb{X}.$$

Let  $\mathbb{X}$  be  $m \times p$  matrix with  $m \geq p$ . Then SVD of  $\mathbb{X}$  is

$$\mathbb{X} = UDV^\top,$$

where  $U_{m \times p}$  has orthonormal columns,  $V_{p \times p}$  is orthogonal, and  $D_{p \times p} = \text{Diag}(d_1, \dots, d_p)$  is diagonal with non-negative elements and  $\cdot$ . Let

$$D^{-} = \text{Diag}(d_1^{-}, \dots, d_p^{-}),$$

where  $d_i^{-} = 1/d_i$  if  $d_i \neq 0$  and  $d_i^{-} = 0$  if  $d_i = 0$ . Then it can be shown that the Moore-Penrose generalized inverse is given by

$$\mathbb{X}^{-} = VD^{-}U^\top.$$

Once we estimated the parameter vector  $\beta$ , the Laplacian of is

$$\Delta\mu(p_0) = 2\hat{\beta}_3 + 2\hat{\beta}_5.$$

## 4 Graph Laplacian

Now we generalize volumetric Laplacian in previous sections to graphs. Let  $G = (V, E)$  be a graph with node set  $V$  and edge set  $E$ . We will simply index the node set as  $V = \{1, 2, \dots, p\}$ . If two nodes  $i$  and  $j$  form an edge, we denote it as  $i \sim j$ . Let  $W = (w_{ij})$  be the edge weight. The adjacency matrix of  $G$  is often used as the edge weight. Various forms of graph Laplacian have been proposed (Chung & Yau 1997) but the most often used standard form  $L = (l_{ij})$  is given by

$$l_{ij} = \begin{cases} -w_{ij}, & i \sim j \\ \sum_{i \neq j} w_{ij}, & i = j \\ 0, & \text{otherwise} \end{cases}$$

Often it is defined with the sign reversed such that

$$l_{ij} = \begin{cases} w_{ij}, & i \sim j \\ -\sum_{i \neq j} w_{ij}, & i = j \\ 0, & \text{otherwise} \end{cases}$$

The graph Laplacian  $L$  can then be written as

$$L = D - W,$$

where  $D = (d_{ij})$  is the diagonal matrix with  $d_{ii} = \sum_{j=1}^n w_{ij}$ . Here, we will simply use the adjacency matrix so that the edge weights  $w_{ij}$  are either 0 or 1. In Matlab, Laplacian  $L$  is simply computed from the adjacency matrix `adj`:

```
n=size(adj,1);
adjsparse = sparse(n,n);
adjsparse(find(adj))=1;
L=sparse(n,n);
GL = inline('diag(sum(W))-W');
L = GL(adjsparse);
```

We use the sparse matrix format to reduce the memory burden for large-scale computation.

**Theorem 3.** *Graph Laplacian  $L$  is nonnegative definite.*

The proof is based on factoring Laplacian  $L$  using incidence matrix  $\nabla$  such that  $L = \nabla^T \nabla$ . Such factorization always yields nonnegative definite matrices. Very often  $L$  is nonnegative definite in practice if it is too sparse (Figure 4).

**Theorem 4.** *For graph Laplacian  $L$ ,  $L + \alpha I$  is positive definite for any  $\alpha > 0$ .*

*Proof.* Since  $L$  is nonnegative definite, we have

$$x^T Lx \geq 0.$$

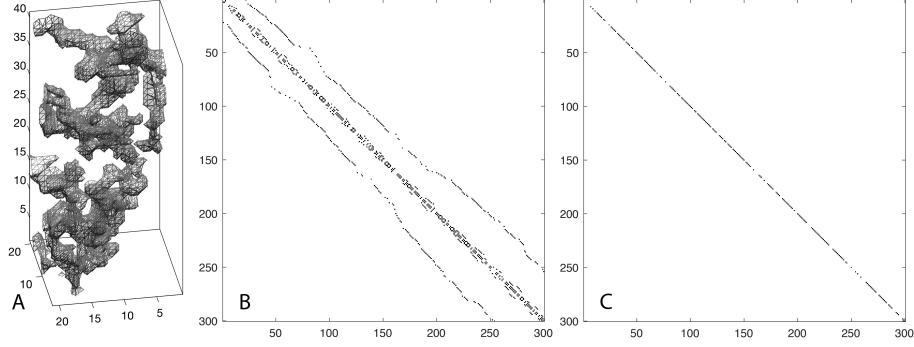


Fig. 4: A. Part of lung blood vessel obtained from CT. B. Adjacency matrix obtained from 4-neighbor connectivity. C. Laplace matrix obtained from the adjacency matrix.

Then it follows that

$$x^\top (L + \alpha I)x = x^\top Lx + \alpha x^\top x > 0$$

for any  $\alpha > 0$  and  $x \neq 0$ .  $\square$

Unlike the continuous Laplace-Beltrami operators that may have possibly infinite number of eigenfunctions, we have up to  $p$  number of eigenvectors  $\psi_1, \psi_2, \dots, \psi_p$  satisfying

$$L\psi_j = \lambda_j \psi_j \quad (15)$$

with (Figure 5)

$$0 = \lambda_1 < \lambda_2 \leq \dots \leq \lambda_p.$$

The eigenvectors are orthonormal, i.e.,

$$\psi_i^\top \psi_j = \delta_{ij},$$

the Kronecker's delta. The first eigenvector is trivially given as  $\psi_1 = \mathbf{1}/\sqrt{p}$  with  $\mathbf{1} = (1, 1, \dots, 1)^\top$ .

All other higher order eigenvalues and eigenvectors are unknown analytically and have to be computed numerically (Figure 5). Using the eigenvalues and eigenvectors, the graph Laplacian can be decomposed spectrally. From (15),

$$L\Psi = \Psi\Lambda, \quad (16)$$

where  $\Psi = [\psi_1, \dots, \psi_p]$  and  $\Lambda$  is the diagonal matrix with entries  $\lambda_1, \dots, \lambda_p$ . Since  $\Psi$  is an orthogonal matrix,

$$\Psi\Psi^\top = \Psi^\top\Psi = \sum_{j=1}^p \psi_j \psi_j^\top = I_p,$$

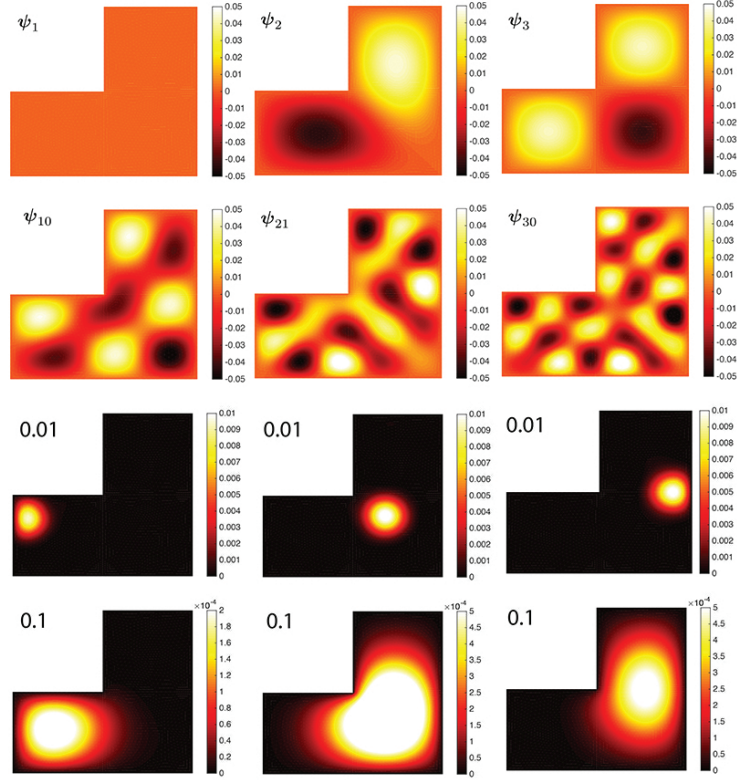


Fig. 5: Top: First few eigenvectors of the Laplacian in a L-shaped domain. Bottom: Heat kernel with bandwidths  $\sigma = 0.01, 0.1$ . We have used degree 70 expansions but the shape is almost identical if we use higher degree expansions. The heat kernel is a probability distribution that follows the shape of the L-shaped domain.

the identify matrix of size  $p$ . Then (16) is written as

$$L = \Psi \Lambda \Psi^\top = \sum_{j=1}^p \lambda_j \psi_j \psi_j^\top.$$

This is the restatement of the singular value decomposition (SVD) for Laplacian.

For measurement vector  $f = (f_1, \dots, f_p)^\top$  observed at the  $p$  nodes, the discrete Fourier series expansion is given by

$$f = \sum_{j=1}^n \tilde{f}_j \psi_j,$$

where  $\tilde{f}_j = f^\top \psi_j = \psi_j^\top f$  are Fourier coefficients.

## 5 Fiedler vectors

The connection between the eigenfunctions of continuous and discrete Laplacians have been well established by many authors (Gladwell & Zhu 2002, Tlustý 2007). Many properties of eigenfunctions of Laplace-Beltrami operator have discrete analogues. The second eigenfunction of the graph Laplacian is called the Fiedler vector and it has been studied in connection to the graph and mesh manipulation, manifold learning and the minimum linear arrangement problem (Fiedler 1973, Ham et al. 2005, Lévy 2006, Ham et al. 2004, 2005).

Let  $G = \{V, E\}$  be the graph with the vertex set  $V$  and the edge set  $E$ . We will simply index the node set as  $V = \{1, 2, \dots, n\}$ . If two nodes  $i$  and  $j$  form an edge, we denote it as  $i \sim j$ . The edge weight between  $i$  and  $j$  is denoted as  $w_{ij}$ . For a measurement vector  $\mathbf{f} = (f_1, \dots, f_n)^\top$  observed at the  $n$  nodes, the discrete Dirichlet energy is given by

$$\mathcal{E}(\mathbf{f}) = \mathbf{f}^\top L \mathbf{f} = \sum_{i,j=1}^n w_{ij} (f_i - f_j)^2 = \sum_{i \sim j} w_{ij} (f_i - f_j)^2. \quad (17)$$

The discrete Dirichlet energy (17) is also called the linear placement cost in the minimum linear arrangement problem (Koren & Harel 2002). Fiedler vector  $\mathbf{f}$  evaluated at  $n$  nodes is obtained as the minimizer of the quadratic polynomial:

$$\min_{\mathbf{f}} \mathcal{E}(\mathbf{f})$$

subject to the quadratic constraint

$$\|\mathbf{f}\|^2 = \mathbf{f}^\top \mathbf{f} = \sum_i f_i^2 = 1. \quad (18)$$

The solution can be interpreted as the kernel principal components of a Gram matrix given by the generalized inverse of  $L$  (Ham et al. 2004, 2005). Since the eigenvector  $\psi_1$  of Laplacian is orthonormal with eigenvector  $\psi_0$ , which is constant, we also have an additional constraint:

$$\sum_i f_i = 0. \quad (19)$$

This optimization problem was first introduced for the minimum linear arrangement problem in 1970's (Hall 1970, Koren & Harel 2002). The optimization can be solved using the Lagrange multiplier as follows (Holzrichter & Oliveira 1999).

Let  $g$  be the constraint (18) so that

$$g(\mathbf{f}) = \mathbf{f}^\top \mathbf{f} - 1 = 0.$$

Then the constrained minimum should satisfy

$$\nabla \mathcal{E} - \mu \nabla g = 0, \quad (20)$$

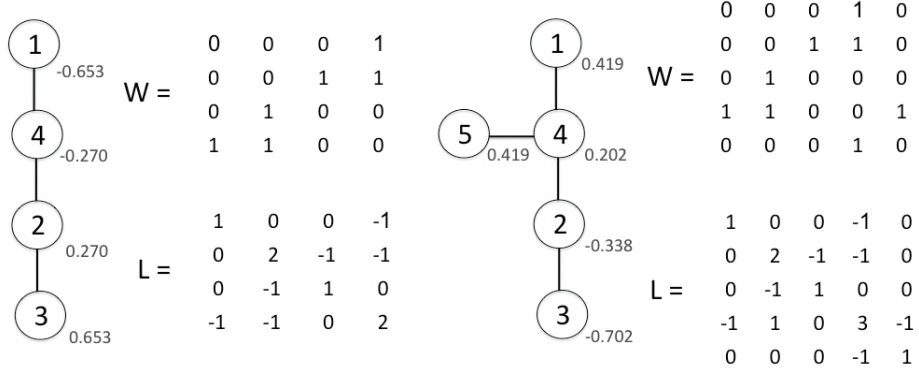


Fig. 6: A weighted graph with weights  $W$  and the graph Laplacian  $L$ . The weights are simply the adjacency matrix. The second eigenvector  $\psi_1$  is given as numbers beside nodes. Left: This example is given in Hall (1970). The maximum geodesic distance is obtained between the nodes 1 and 3, which are also hot and cold spots. Right: There are two hot spots 1 and 5 which corresponds to two maximal geodesic paths 1-4-2-3 and 5-4-2-3 (Chung et al. 2011).

where  $\mu$  is the Lagrange multiplier. (20) can be written as

$$2L\mathbf{f} - \mu\mathbf{f} = 0 \quad (21)$$

Hence,  $\mathbf{f}$  must be the eigenvector of  $L$  and  $\mu/2$  is the corresponding eigenvalue. By multiplying  $\mathbf{f}^\top$  on the both sides of (21), we have

$$2\mathbf{f}^\top L\mathbf{f} = \mu\mathbf{f}^\top \mathbf{f} = \mu.$$

Since we are minimizing  $\mathbf{f}^\top L\mathbf{f}$ ,  $\mu/2$  should be the second eigenvalue  $\lambda_1$ .

In most literature (Holzrichter & Oliveira 1999), the condition  $\sum_i f_i = 0$  is incorrectly stated as a necessary constraint for the Fiedler vector. However, the constraint  $\sum_i f_i = 0$  is not really needed in minimizing the Dirichlet energy. This can be further seen from introducing a new constraint

$$h(\mathbf{f}) = \mathbf{e}^\top \mathbf{f} = \sum_i f_i = 0,$$

where  $\mathbf{e} = (1, \dots, 1)^\top$ .

The constraint (18) and (19) forces  $\psi_1$  to have at least two differing *sign domains* in which  $\psi_1$  has one sign. But it is unclear how many differing sign domains  $\psi_1$  can possibly have. The upper bound is given by Courant's nodal line theorem (Courant & Hilbert 1953, Gladwell & Zhu 2002, Tlustý 2007). The *nodal set* of eigenvector  $\psi_i$  is defined as the zero level set  $\psi_i(p) = 0$ . Courant's nodal line theorem states that the nodal set of the  $i$ -th eigenvector  $\psi_i$  divides the graph into no more than  $i$  sign domains. Hence, the second eigenvector has exactly 2 disjoint sign domains. At the positive sign domain, we have the global maximum

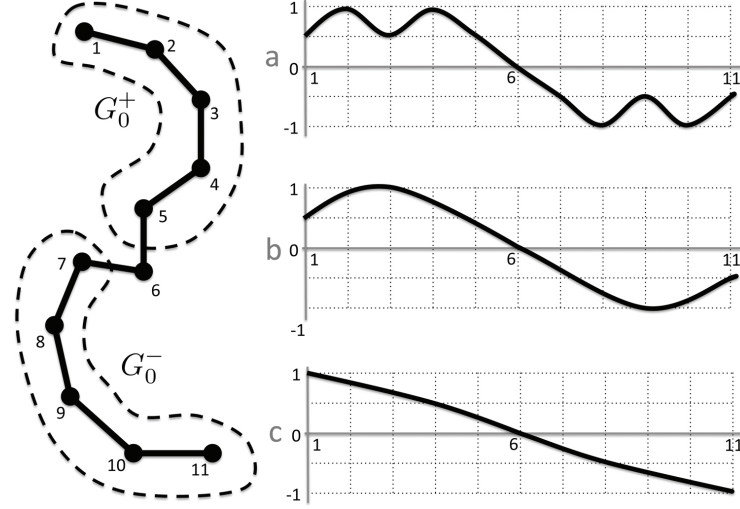


Fig. 7: A path with with positive ( $G_0^+$ ) and negative ( $G_0^-$ ) sign domains. Due to symmetry, the possible eigenfunction  $\psi_1$  has to be an odd function.

and at the negative sign domain, we have the global minimum. This property is illustrated in Figure 6. However, it is unclear where the global maximum and minimum are located. The concept of tightness is useful in determining the location.

**Definition 1.** For a function  $\mathbf{f}$  defined on vertex set  $V$  of  $G$ , let  $G_s^-$  be the subgraph of  $G$  induced by the vertex set  $V_s^- = \{i \in V | f_i < s\}$ . Let  $G_s^+$  be the subgraph of  $G$  induced by the vertex set  $V_s^+ = \{i \in V | f_i > s\}$ . For any  $s$ , if  $G_s^-$  and  $G_s^+$  are either connected or empty, then  $\mathbf{f}$  is tight (Tlustý 2007).

When  $s = 0$ ,  $G_0^+$  and  $G_0^-$  are sign graphs. If we relax the condition so that  $G_s^+$  contains nodes satisfying  $f_i \geq s$ , we have weak sign graphs. It can be shown that the second eigenvector on a graph with maximal degree 2 (cycle or path) is tight (Tlustý 2007). Figure 7 shows an example of a path with 11 nodes. Among three candidates for the second eigenfunction, (a) and (b) are not tight while (c) is. Note that the candidate function (a) has two disjoint components for  $G_{0.5}^+$  so it can not be tight. In order to be tight, the second eigenfunction cannot have a positive minimum or a negative maximum at the interior vertex in the graph (Gladwell & Zhu 2002). This implies that the second eigenfunction must decrease monotonically from the positive to negative sign domains as shown in (c). Therefore, the hot and cold spots must occur at the two end points 1 and 11, which gives the maximum geodesic distance of 11.

For a cycle, the argument is similar except that a possible eigenfunction has to be periodic and tight, which forces the hot and cold spots to be located at the maximum distance apart. Due to the periodicity, we will have multiplicity

of eigenvalues in the cycle. Although it is difficult to predict the location of maximum and minimums in general, the behavior of the second eigenfunction is predictable for an elongated graph; it provides an intrinsic geometric way of establishing natural coordinates.

## 6 Heat kernel smoothing on graphs

*Heat kernel smoothing* was originally introduced in the context of filtering out cortical surface data defined on mesh vertices obtained from 3D medical images (Chung, Robbins & Evans 2005, Chung, Robbins, Dalton, Davidson, Alexander & Evans 2005). The formulation uses the tangent space projection in approximating the heat kernel by iteratively applying Gaussian kernel with smaller bandwidth. Recently proposed spectral formulation to heat kernel smoothing (Chung et al. 2015) constructs the heat kernel analytically using the eigenfunctions of the Laplace-Beltrami (LB) operator, avoiding the need for the linear approximation used in (Chung, Robbins & Evans 2005, Han et al. 2006). Since surface meshes are graphs, heat kernel smoothing can be used to smooth noisy data defined on network nodes.

Instead of Laplace-Beltrami operator for cortical surface, graph Laplacian is used to construct the discrete version of heat kernel smoothing. The connection between the eigenfunctions of continuous and discrete Laplacians has been well established by several studies (Gladwell & Zhu 2002, Tlusty 2007). Although many have introduced the discrete version of heat kernel in computer vision and machine learning, they mainly used the heat kernels to compute shape descriptors or to define a multi-scale metric (Belkin et al. 2006, Sun et al. 2009, Bronstein & Kokkinos 2010, de Goes et al. 2008). These studies did not use the heat kernel in filtering out data on graphs. There have been significant developments in kernel methods in the machine learning community (Schölkopf & Smola 2002, Nilsson et al. 2007, Shawe-Taylor & Cristianini 2004, S. & H. 2008, Yger & Rakotomamonjy 2011). However, the heat kernel has never been used in such frameworks. Most kernel methods in machine learning deal with the linear combination of kernels as a solution to penalized regressions. On the other hand, our kernel method does not have a penalized cost function.

### 6.1 Heat kernel on graphs

The *discrete heat kernel*  $K_\sigma$  is a positive definite symmetric matrix of size  $p \times p$  given by

$$K_\sigma = \sum_{j=1}^p e^{-\lambda_j \sigma} \psi_j \psi_j^\top, \quad (22)$$

where  $\sigma$  is called the bandwidth of the kernel. Figure 5 displays heat kernel with different bandwidths at a L-shaped domain. Alternately, we can write (22) as

$$K_\sigma = \Psi e^{-\sigma \Lambda} \Psi^\top,$$

where  $e^{-\sigma A}$  is the matrix logarithm of  $A$ . To see positive definiteness of the kernel, for any nonzero  $x \in \mathbb{R}^p$ ,

$$\begin{aligned} x^\top K_\sigma x &= \sum_{j=1}^p e^{-\lambda_j \sigma} x^\top \psi_j \psi_j^\top x \\ &= \sum_{j=1}^p e^{-\lambda_j \sigma} (\psi_j^\top x)^2 > 0. \end{aligned}$$

When  $\sigma = 0$ ,  $K_0 = I_p$ , identity matrix. When  $\sigma = \infty$ , by interchanging the sum and the limit, we obtain

$$K_\infty = \psi_1 \psi_1^\top = \mathbf{1} \mathbf{1}^\top / p.$$

$K_\infty$  is a degenerate case and the kernel is no longer positive definite. Other than these specific cases, the heat kernel is not analytically known in arbitrary graphs.

Heat kernel is doubly-stochastic (Chung & Yau 1997) so that

$$K_\sigma \mathbf{1} = \mathbf{1}, \quad \mathbf{1}^\top K_\sigma = \mathbf{1}^\top.$$

Thus,  $K_\sigma$  is a probability distribution along columns or rows.

Just like the continuous counterpart, the discrete heat kernel is also multiscale and has the scale-space property. Note

$$\begin{aligned} K_\sigma^2 &= \sum_{i,j=1}^p e^{-(\lambda_i + \lambda_j)\sigma} \psi_i \psi_i^\top \psi_j \psi_j^\top \\ &= \sum_{j=1}^p e^{-2\lambda_j \sigma} \psi_j \psi_j^\top = K_{2\sigma}. \end{aligned}$$

We used the orthonormality of eigenvectors. Subsequently, we have

$$K_\sigma^n = K_{n\sigma}.$$

## 6.2 Heat kernel smoothing on graphs

Discrete heat kernel smoothing of measurement vector  $f$  is then defined as convolution

$$K_\sigma * f = K_\sigma f = \sum_{j=0}^p e^{-\lambda_j \sigma} \tilde{f}_j \psi_j, \quad (23)$$

This is the discrete analogue of heat kernel smoothing first defined in (Chung, Robbins & Evans 2005). In discrete setting, the convolution  $*$  is simply a matrix multiplication. Thus,

$$K_0 * f = f$$

and

$$K_\infty * f = \bar{f}\mathbf{1},$$

where  $\bar{f} = \sum_{j=1}^p f_j/p$  is the mean of signal  $f$  over every nodes. When the bandwidth is zero, we are not smoothing data. As the bandwidth increases, the smoothed signal converges to the sample mean over all nodes.

Define the  $l$ -norm of a vector  $f = (f_1, \dots, f_p)^\top$  as

$$\|f\|_l = \left( \sum_{j=1}^p |f_j|^l \right)^{1/l}.$$

The matrix  $\infty$ -norm is defined as

$$\|f\|_\infty = \max_{1 \leq j \leq p} |f_j|.$$

**Theorem 5.** *Heat kernel smoothing is a contraction mapping with respect to the  $l$ -th norm, i.e.,*

$$\|K_\sigma * f\|_l^l \leq \|f\|_l^l.$$

*Proof.* Let kernel matrix  $K_\sigma = (k_{ij})$ . Then we have inequality

$$\|K_\sigma * f\|_l^l = \sum_{i=1}^p \sum_{j=1}^p |k_{ij} f_j|^l \leq \sum_{j=1}^p |f_j|^l.$$

We used Jensen's inequality and doubly-stochastic property of heat kernel. Similarly, we can show that heat kernel smoothing is a contraction mapping with respect to the  $\infty$ -norm as well.

Theorem 1 shows that heat kernel smoothing contracts the overall size of data. This fact can be used to skeltonize the blood vessel trees.

### 6.3 Statistical properties

Often observed noisy data  $f$  on graphs is smoothed with heat kernel  $K_\sigma$  to increase the signal-to-noise ratio (SNR) and increases the statistical sensitivity (Chung et al. 2015). We are interested in knowing how heat kernel smoothing will affect on the statistical properties of smoothed data.

Consider the following additive noise model:

$$f = \mu + e, \tag{24}$$

where  $\mu$  is unknown signal and  $e$  is zero mean noise. Let  $e = (e_1, \dots, e_p)^\top$ . Denote  $\mathbb{E}$  as expectation and  $\mathbb{V}$  as covariance. It is natural to assume that the noise variabilities at different nodes are identical, i.e.,

$$\mathbb{E}e_1^2 = \mathbb{E}e_2^2 = \dots = \mathbb{E}e_p^2. \tag{25}$$

Further, we assume that data at two nodes  $i$  and  $j$  to have less correlation when the distance between the nodes is large. So covariance matrix

$$R_e = \mathbb{V}e = \mathbb{E}(ee^\top) = (r_{ij})$$

can be given by

$$r_{ij} = \rho(d_{ij}) \quad (26)$$

for some decreasing function  $\rho$  and geodesic distance  $d_{ij}$  between nodes  $i$  and  $j$ . Note  $r_{jj} = \rho(0)$  with the understanding that  $d_{jj} = 0$  for all  $j$ . The off-diagonal entries of  $R_e$  are smaller than the diagonals.

Noise  $e$  can be further modeled as Gaussian white noise, i.e., Brownian motion or the generalized derivatives of Wiener process, whose covariance matrix elements are Dirac-delta. For the discrete counterpart,  $r_{ij} = \delta_{ij}$ , where  $\delta_{ij}$  is Kroneker-delta with  $\delta_{ij} = 1$  if  $i = j$  and 0 otherwise. Thus,

$$R_e = \mathbb{E}(ee^\top) = I_p,$$

the identity matrix of size  $p \times p$ . Since  $\delta_{jj} \geq \delta_{ij}$ , Gaussian white noise is a special case of (26).

Once heat kernel smoothing is applied to (24), we have

$$K_\sigma * f = K_\sigma * \mu + K_\sigma * e. \quad (27)$$

We are interested in knowing how the statistical properties of model change from (24) to (27). For  $R_e = I_p$ , the covariance matrix of smoothed noise is simply given as

$$R_{K_\sigma * e} = K_\sigma \mathbb{E}(ee^\top) K_\sigma = K_\sigma^2 = K_{2\sigma}.$$

We used the scale-space property of heat kernel. In general, the covariance matrix of smoothed data  $K_\sigma * e$  is given by

$$R_{K_\sigma * e} = K_\sigma \mathbb{E}(ee^\top) K_\sigma = K_\sigma R_e K_\sigma.$$

The variance of data will be often reduced after heat kernel smoothing in the following sense (Chung, Robbins & Evans 2005, Chung, Robbins, Dalton, Davidson, Alexander & Evans 2005):

**Theorem 6.** *Heat kernel smoothing reduces variability, i.e.,*

$$\mathbb{V}(K_\sigma * f)_j \leq \mathbb{V}f_j$$

for all  $j$ . The subscript  $j$  indicates the  $j$ -th element of the vector.

*Proof.* Note

$$\mathbb{V}(K_\sigma * f)_j = \mathbb{V}(K_\sigma * e)_j = \mathbb{E}\left(\sum_{i=1}^p k_{ij} e_i\right)^2.$$

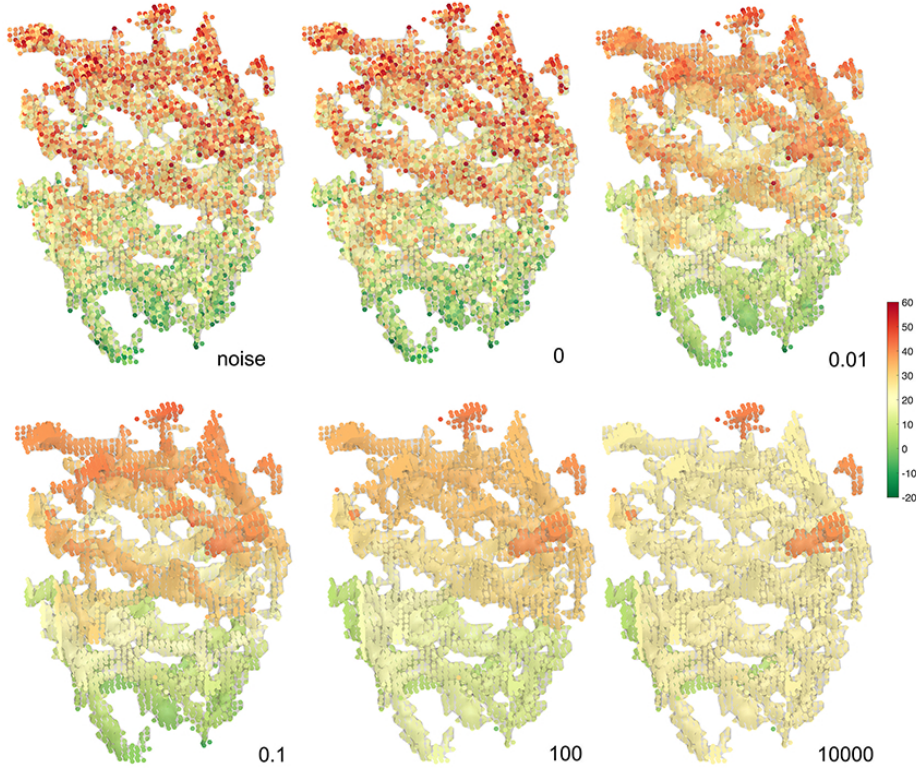


Fig. 8: From top left to right: 3D lung vessel tree. Gaussian noise is added to one of the coordinates. 3D graph constructed using 6-connected neighbors. The numbers are the kernel bandwidth  $\sigma$ .

Since  $(k_{ij})$  is doubly-stochastic, after applying Jensen's inequality, we obtain

$$\mathbb{E}\left(\sum_{i=1}^p k_{ij}e_i\right)^2 \leq \mathbb{E}\left(\sum_{i=1}^p k_{ij}e_i^2\right) = \mathbb{E}e_i^2.$$

For the last equality, we used the equality of noise variability (25). Since  $\mathbb{E}f_j = \mathbb{E}e_i^2$ , we proved the statement.  $\square$

Theorem 6 shows that the variability of data decreases after heat kernel smoothing.

#### 6.4 Skeleton representation using heat kernel smoothing

Discrete heat kernel smoothing can be used to smooth out and present very complex patterns and get the skeleton representation. Here, we show how it is applied to the 3D graph obtained from the computed tomography (CT) of human lung vessel trees (Chung et al. 2018, Castillo et al. 2009, Wu et al. 2013). In this

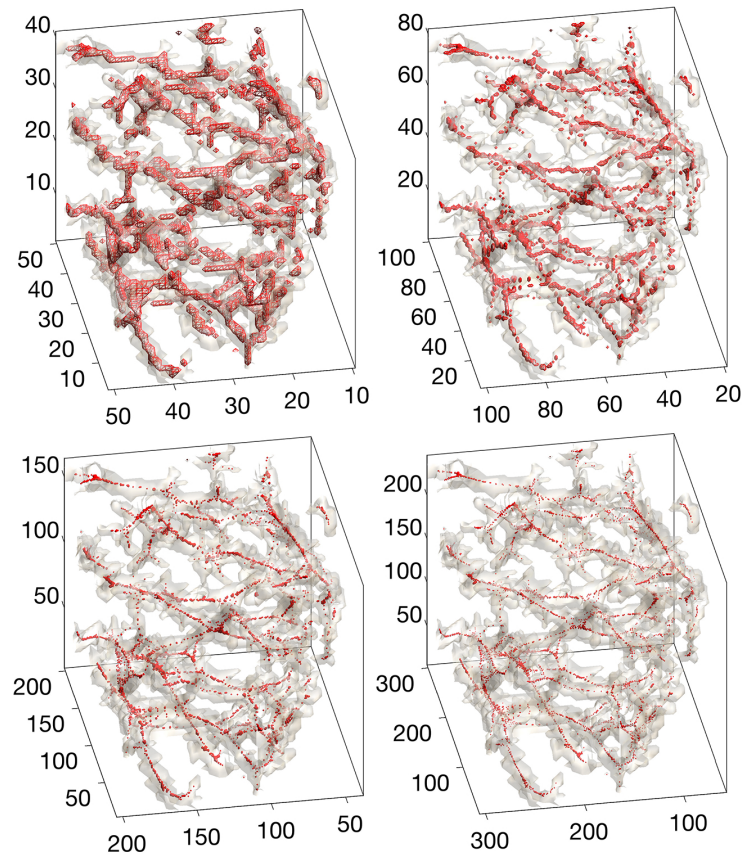


Fig. 9: The skeleton representation of vessel trees. Using the heat kernel series expansion with bandwidth  $\sigma = 1$  and 6000 basis, we upsampled the binary segmentation at 2, 4, 6 times (clockwise from top right) larger than the original size (top left).

example, the 3D binary vessel segmentation from CT was obtained using the multiscale Hessian filters at each voxel (Frangi et al. 1998, Korfiatis et al. 2011, Shang et al. 2011). The binary segmentation was converted into a 3D graph by taking each voxel as a node and connecting neighboring voxels. Using the 18-connected neighbor scheme, we connect two voxels only if they touch each other on their faces or edges. If voxels are only touching at their corner vertices, they are not considered as connected. If the 6-connected neighbor scheme is used, we will obtain far sparse adjacency matrix and corresponding graph Laplacian. The eigenvector of graph Laplacian is obtained using an Implicitly Restarted Arnoldi Iteration method (Lehoucq & Sorensen 1996). We used 6000 eigenvectors. Note we cannot have more eigenvectors than the number of nodes.

As an illustration, we performed heat kernel smoothing on simulated data. Gaussian noise is added to one of the coordinates (Figure 8). Heat kernel smoothing is performed on the noise added coordinate. Numbers in Figure 8 are kernel bandwidths. At  $\sigma = 0$ , heat kernel smoothing is equivalent to Fourier series expansion. Thus, we get the almost identical result. As the bandwidth increases, smoothing converges to the mean value. Each disconnected regions should converge to their own different mean values. Thus, when  $\sigma = 10000$ , the regions that are different colors are regions that are disconnected. This phenomena is related to the hot spots conjecture in differential geometry (Banuelos & Burdzy 1999, Chung et al. 2011). The number of disconnected structures can be obtained counting the zero eigenvalues.

The technique can be used to extract the skeleton representation of vessel trees. We perform heat kernel smoothing on node coordinates with  $\sigma = 1$ . Then rounded off the smoothed coordinates to the nearest integers. The rounded off coordinates were used to reconstruct the binary segmentation. This gives the thick trees in Figure 9 (top left). To obtain thinner trees, the smoothed coordinates were scaled by the factor of 2, 4 and 6 times before rounding off. This had the effect of increasing the image size relative to the kernel bandwidth thus obtaining the skeleton representation of the complex blood vessel (Figure 9 clockwise from top right) (Lindvere et al. 2013, Cheng et al. 2014). By connecting the voxels sequentially, we can obtain the graph representation of the skeleton as well. The method can be easily adopted for obtaining the skeleton representation of complex brain network patterns.

### 6.5 Diffusion wavelets

Consider a traditional wavelet basis  $W_{t,q}(p)$  obtained from a mother wavelet  $W$  with scale and translation parameters  $t$  and  $q$  in Euclidean space (Kim et al. 2012):

$$W_{t,q}(p) = \frac{1}{t} W\left(\frac{p-q}{t}\right). \quad (28)$$

The wavelet transform of a signal  $f(p)$  is given by kernel

$$\langle W_{t,q}, f \rangle = \int_{\mathcal{M}} W_{t,q}(p) f(p) d\mu(p).$$

Scaling a function on an arbitrary manifold including graph is trivial. But the difficulty arises when one tries to translate a mother wavelet. It is not straightforward to generalize the Euclidean formulation (28) to an arbitrary manifold, due to the lack of regular grids (Nain et al. 2007, Bernal-Rusiel et al. 2008). The recent work based on the diffusion wavelet bypasses this problem also by taking bivariate kernel as a mother wavelet (Antoine et al. 2010, Hammond et al. 2011, Mahadevan & Maggioni 2006, Kim et al. 2012). By simply changing the second argument of the kernel, it has the effect of translating the kernel. The diffusion wavelet construction has been fairly involving so far. However, it can be shown

to be a special case of the heat kernel regression with proper normalization. Following the notations in Antoine et al. (2010), Hammond et al. (2011), Kim et al. (2012), diffusion wavelet  $W_{t,q}(p)$  at position  $p$  and scale  $t$  is given by

$$W_{t,q}(p) = \sum_{j=0}^k g(\lambda_j t) \psi_j(p) \psi_j(q),$$

for some scale function  $g$ . If we let  $\tau_j = g(\lambda_j t)$ , the diffusion wavelet transform is given by

$$\begin{aligned} \langle W_{t,q}, f \rangle &= \int_{\mathcal{M}} W_{t,q}(p) f(p) d\mu(p) \\ &= \sum_{j=0}^k g(\lambda_j t) \psi_j(q) \int_{\mathcal{M}} f(p) \psi_j(p) d\mu(p) \\ &= \sum_{j=0}^k \tau_j f_j \psi_j(q), \end{aligned} \tag{29}$$

where  $f_j = \langle f, \psi_j \rangle$  is the Fourier coefficient. Note (29) is the kernel regression (Chung et al. 2015). Hence, the diffusion wavelet transform can be simply obtained by doing the kernel regression without an additional wavelet machinery as done in Kim et al. (2012). Further, if we let  $g(\lambda_j t) = e^{-\lambda_j t}$ , we have

$$W_{t,p}(q) = \sum_{j=0}^k e^{-\lambda_j t} \psi_j(p) \psi_j(q),$$

which is a heat kernel. The bandwidth  $t$  of heat kernel controls resolution while the translation is done by shifting one argument in the kernel.

## 7 Laplace equation

In this section, we will show how to solve for steady state of diffusion. The distribution of fictional charges within the two boundaries sets up a scalar potential field  $f$ , which satisfies the Poisson equation

$$\Delta f = \frac{\partial^2 f}{\partial x^2} + \frac{\partial^2 f}{\partial y^2} + \frac{\partial^2 f}{\partial z^2} = \frac{\rho}{\epsilon_0},$$

where  $\rho$  is the total charge within the boundaries. If we set up the two boundaries at different potential, say at  $f_0$  and  $f_1$ , without enclosing any charge, we have the Laplace equation

$$\Delta f = 0.$$

The Laplace equation can be viewed as the steady state of diffusion

$$\frac{df(t,p)}{dt} = \Delta f$$

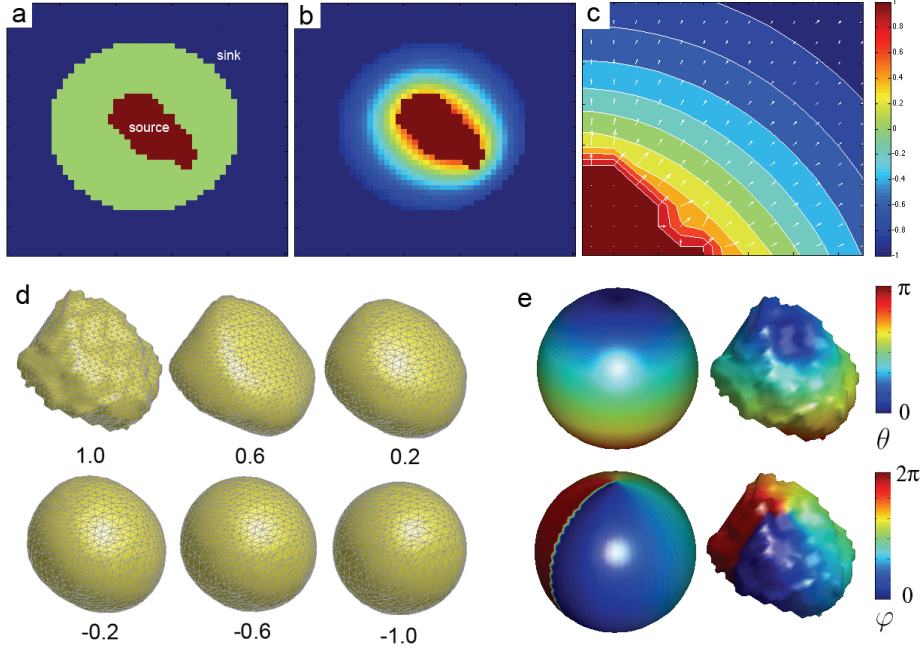


Fig. 10: (a) The heat source (amygdala) is assigned value 1 while the heat sink (outer sphere) is assigned the value -1. The diffusion equation is solved with these boundary conditions. (b) After a sufficient number of iterations, the equilibrium state  $f(\infty, p)$  is reached. (c) The gradient field  $\nabla f(t = \infty, p)$  shows the direction of heat propagation from the source to the sink. The integral curve of the gradient field is computed by connecting one level set to the next level set of  $f(\infty, p)$ . (d) The deformation of amygdala surface to the sphere is done by tracing the integral curve at each mesh vertex. The numbers  $c = 1.0, 0.6, \dots, -1.0$  correspond to the level sets  $f(\infty, p)$ . (e) The surface flattening to the sphere produces the surface parameterization based on the spherical angles  $(\theta, \varphi)$ . The point  $\theta = 0$  corresponds to the north pole of a unit sphere. The method presented here is published in (Chung et al. 2010, Chung 2012).

when  $t \rightarrow \infty$ . By solving the Laplace equation with the two boundary conditions, we obtain the potential field  $f$ . Then the electric field perpendicular to the isopotential surfaces is given by  $-\nabla f$ . The Laplace equation is mainly solved using the finite difference scheme (Chung 2012). The electric field lines radiate from one conducting surface to the other without crossing each other. By tracing the electric field lines, we obtain one-to-one smooth map between surfaces (Figure 10). The underlying framework is identical to the Laplace equation based surface flattening or cortical thickness estimation (Jones et al. 2000, Chung et al. 2010).

### 7.1 Galerkin's method for solving Laplace equation

Without using the finite difference scheme, we can use an analytic approach for solving the Laplace equation using Galerkin's method (Kirby 2000). Galerkin's method discretizes partial differential equations and integral equations as a collection of linear equations involving basis functions. The linear equations are then usually solved in the least squares fashion. The iterative residual fitting (IRF) algorithm (Chung et al. 2007, 2008), which iteratively fits functional data using diffusion equations, can be considered as a special case of Galerkin's method.

We assume the eigenfunctions of  $\Delta$  satisfying

$$\Delta\psi_j = \lambda_j\psi_j$$

are available. The solution of the Laplace equation is then approximated as a finite expansion

$$f(p) = \sum_{j=0}^k c_j\psi_j(p).$$

Consider following boundary conditions

$$f(p) = 1, p \in G_+, \text{ and } f(p) = -1, p \in G_-, \quad (30)$$

where  $G_+$  and  $G_-$  are the subregions of  $G$ .  $G_+$  and  $G_-$  can be 3D objects, 2D surfaces, graphs or networks. The integral curve between  $G_+$  and  $G_-$  will establish one to one correspondence.

The boundary conditions satisfy

$$1 = \sum_{j=0}^k c_j\psi_j(p_{2i}), p_{2i} \in G_+ \quad (31)$$

and

$$-1 = \sum_{j=0}^k c_j\psi_j(p_{3i}), p_{3i} \in G_-. \quad (32)$$

In the interior region  $G \setminus (G_+ \cup G_-)$ , by taking the Laplacian on the expansion  $f(p) = \sum_{j=0}^k c_j\psi_j(p)$ , we have

$$0 = \sum_{j=0}^k c_j\Delta\psi_j(p_{1i}) = \sum_{j=0}^k c_j\lambda_j\psi_j(p_{1i}), p_{1i} \in G \setminus (G_+ \cup G_-). \quad (33)$$

We assume that there are  $a, b$  and  $c$  number of points for equations (31), (32) and (33) respectively. We now combine linear equations (31), (32) and (33)

together in a matrix form:

$$\underbrace{\begin{pmatrix} 0 \\ \vdots \\ 0 \\ 1 \\ \vdots \\ 1 \\ -1 \\ \vdots \\ -1 \end{pmatrix}}_{\mathbf{y}} = \underbrace{\begin{pmatrix} \lambda_0 \psi_0(p_{11}) & \cdots & \lambda_k \psi_k(p_{11}) \\ \vdots & \ddots & \vdots \\ \lambda_0 \psi_0(p_{1a}) & \cdots & \lambda_k \psi_k(p_{1a}) \\ \psi_0(p_{21}) & \cdots & \psi_k(p_{21}) \\ \vdots & \ddots & \vdots \\ \psi_0(p_{2b}) & \cdots & \psi_k(p_{2b}) \\ \psi_0(p_{31}) & \cdots & \psi_k(p_{31}) \\ \vdots & \ddots & \vdots \\ \psi_0(p_{3c}) & \cdots & \psi_k(p_{3c}) \end{pmatrix}}_{\mathbf{\Psi}} \underbrace{\begin{pmatrix} c_0 \\ c_1 \\ \vdots \\ c_{k-1} \\ c_k \end{pmatrix}}_{\mathbf{C}}. \quad (34)$$

The size of matrix  $\mathbf{\Psi}$  is  $(a + b + c) \times (1 + k)$ .  $\mathbf{\Psi}'\mathbf{\Psi}$  is invertible if we sample substantially large number of points  $a + b + c \gg k$ . This is likely to be true in medical images so there is no need to use the pseudo-inverse here. Then the matrix equation can be solved by the least squares method:

$$\hat{\mathbf{C}} = (\mathbf{\Psi}'\mathbf{\Psi})^{-1}\mathbf{\Psi}\mathbf{y}.$$

## 7.2 Laplace equation with graphs

We can solve for the Laplace equation within a graph  $G$ . We pick  $G_+$  and  $G_-$  to be subgraphs of  $G$ . For instance, we can take  $G_+$  and  $G_-$  at the two nodes in the graph and solve for the Laplace equation. With the boundary condition  $f(G_+) = 1$  and  $f(G_-) = 1$ , we are basically solving for steady state heat diffusion between heat source  $G_+$  and heat sink  $G_-$ .

Instead of solving the Laplace equation within a graph, we can also solve it between graphs by taking  $G_+$  and  $G_-$  to be two different graphs. For instance, we can take two correlation matrices  $G_+ = (g_{ij}^+)$  and  $G_- = (g_{ij}^-)$ , which can be viewed as weighted complete graphs. If we take  $\Delta$  as the Hodge Laplacian defined on edges (Anand et al. 2021), we can solve the Laplace equation with two correlation matrices as boundary conditions. This provides smooth one-to-one mapping between two correlation matrices. Unlike the usual element wise matching of  $g_{ij}^+$  and  $g_{ij}^-$ , it provides the mapping through heat flow.

## Acknowledgements

The part of this study was supported by NIH grants NIH R01 EB022856 and R01 EB028753, NSF grant MDS-2010778. We would like to thank Yuan Wang of University of South Carolina for the providing Gibbs phenomenon plot and Gurong Wu of University of North Carolina for providing lung CT scans.

## Bibliography

- Anand, D., Dakurah, S., Wang, B. & Chung, M. (2021), ‘Hodge-Laplacian of brain networks and its application to modeling cycles’, *arXiv preprint 2110.14599*.
- Andrade, A., Kherif, F., Mangin, J., Worsley, K., Paradis, A., Simon, O., Dehaene, S., Le Bihan, D. & Poline, J.-B. (2001), ‘Detection of fMRI activation using cortical surface mapping’, *Human Brain Mapping* **12**, 79–93.
- Antoine, J.-P., Roşca, D. & Vandergheynst, P. (2010), ‘Wavelet transform on manifolds: old and new approaches’, *Applied and Computational Harmonic Analysis* **28**, 189–202.
- Banuelos, R. & Burdzy, K. (1999), ‘On the Hot Spots Conjecture of J Rauch’, *Journal of Functional Analysis* **164**, 1–33.
- Belkin, M., Niyogi, P. & Sindhwani, V. (2006), ‘Manifold regularization: A geometric framework for learning from labeled and unlabeled examples’, *The Journal of Machine Learning Research* **7**, 2399–2434.
- Bernal-Rusiel, J., Atienza, M. & Cantero, J. (2008), ‘Detection of focal changes in human cortical thickness: Spherical wavelets versus gaussian smoothing’, *NeuroImage* **41**, 1278–1292.
- Bronstein, M. M. & Kokkinos, I. (2010), Scale-invariant heat kernel signatures for non-rigid shape recognition, in ‘IEEE Conference on Computer Vision and Pattern Recognition (CVPR)’, pp. 1704–1711.
- Bulow, T. (2004), ‘Spherical diffusion for 3D surface smoothing’, *IEEE Transactions on Pattern Analysis and Machine Intelligence* **26**, 1650–1654.
- Cachia, A., Mangin, J.-F., Rivière, D., Kherif, F., Boddaert, N., Andrade, A., Papadopoulos-Orfanos, D., Poline, J.-B., Bloch, I., Zilbovicius, M., Sonigo, P., Brunelle, F. & Régis, J. (2003), ‘A primal sketch of the cortex mean curvature: A morphogenesis based approach to study the variability of the folding patterns’, *IEEE Transactions on Medical Imaging* **22**, 754–765.
- Cachia, A., Mangin, J.-F., Rivière, D., Papadopoulos-Orfanos, D., Kherif, F., Bloch, I. & Régis, J. (2003), ‘A generic framework for parcellation of the cortical surface into gyri using geodesic Voronoï diagrams’, *Image Analysis* **7**, 403–416.
- Castillo, R., Castillo, E., Guerra, R., Johnson, V., McPhail, T., Garg, A. & Guerrero, T. (2009), ‘A framework for evaluation of deformable image registration spatial accuracy using large landmark point sets’, *Physics in medicine and biology* **54**, 1849–1870.
- Cheng, L., De, J., Zhang, X., Lin, F. & Li, H. (2014), Tracing retinal blood vessels by matrix-forest theorem of directed graphs, in ‘International Conference on Medical Image Computing and Computer Assisted Intervention’, Springer, pp. 626–633.
- Chung, F. & Yau, S. (1997), ‘Eigenvalue inequalities for graphs and convex subgraphs’, *Communications in Analysis and Geometry* **5**, 575–624.

- Chung, M. (2001), *Statistical Morphometry in Neuroanatomy*, Ph.D. Thesis, McGill University. <http://www.stat.wisc.edu/~mchung/papers/thesis.pdf>.
- Chung, M. (2012), *Computational Neuroanatomy: The Methods*, World Scientific, Singapore.
- Chung, M., Dalton, K., Shen, L., Evans, A. & Davidson, R. (2007), ‘Weighted Fourier representation and its application to quantifying the amount of gray matter’, *IEEE Transactions on Medical Imaging* **26**, 566–581.
- Chung, M., Hartley, R., Dalton, K. & Davidson, R. (2008), ‘Encoding cortical surface by spherical harmonics’, *Statistica Sinica* **18**, 1269–1291.
- Chung, M., Qiu, A., Seo, S. & Vorperian, H. (2015), ‘Unified heat kernel regression for diffusion, kernel smoothing and wavelets on manifolds and its application to mandible growth modeling in CT images’, *Medical Image Analysis* **22**, 63–76.
- Chung, M., Robbins, S., Dalton, K., Davidson, R., Alexander, A. & Evans, A. (2005), ‘Cortical thickness analysis in autism with heat kernel smoothing’, *NeuroImage* **25**, 1256–1265.
- Chung, M., Robbins, S. & Evans, A. (2005), ‘Unified statistical approach to cortical thickness analysis’, *Information Processing in Medical Imaging (IPMI), Lecture Notes in Computer Science* **3565**, 627–638.
- Chung, M., Seo, S., Adluru, N. & Vorperian, H. (2011), ‘Hot spots conjecture and its application to modeling tubular structures’, in ‘International Workshop on Machine Learning in Medical Imaging’, Vol. 7009, pp. 225–232.
- Chung, M. & Taylor, J. (2004), ‘Diffusion smoothing on brain surface via finite element method’, in ‘Proceedings of IEEE International Symposium on Biomedical Imaging (ISBI)’, Vol. 1, pp. 432–435.
- Chung, M., Wang, Y. & Wu, G. . (2018), ‘Heat kernel smoothing in irregular image domains’, *International Conference of the IEEE Engineering in Medicine and Biology Society (EMBC)* pp. 5101–5104.
- Chung, M., Worsley, K., Brendon, M., Dalton, K. & Davidson, R. (2010), ‘General multivariate linear modeling of surface shapes using SurfStat’, *NeuroImage* **53**, 491–505.
- Chung, M., Worsley, K., Robbins, S. & Evans, A. (2003), ‘Tensor-based brain surface modeling and analysis’, in ‘IEEE Conference on Computer Vision and Pattern Recognition (CVPR)’, Vol. I, pp. 467–473.
- Chung, M., Worsley, K., Robbins, S., Paus, T., Taylor, J., Giedd, J., Rapoport, J. & Evans, A. (2003), ‘Deformation-based surface morphometry applied to gray matter deformation’, *NeuroImage* **18**, 198–213.
- Chung, M., Worsley, K., Taylor, J., Ramsay, J., Robbins, S. & Evans, A. (2001), ‘Diffusion smoothing on the cortical surface’, *NeuroImage* **13**, S95.
- Courant, R. & Hilbert, D. (1953), *Methods of Mathematical Physics*, English edn, Interscience, New York.
- de Goes, F., Goldenstein, S. & Velho, L. (2008), ‘A hierarchical segmentation of articulated bodies’, *Computer Graphics Forum* **27**, 1349–1356.
- Fiedler, M. (1973), ‘Algebraic connectivity of graphs’, *Czechoslovak Mathematical Journal* **23**, 298–305.

- Frangi, A., Niessen, W., Vincken, K. & Viergever, M. (1998), Multiscale vessel enhancement filtering, in ‘International Conference on Medical Image Computing and Computer-Assisted Intervention’, Vol. 1496, pp. 130–137.
- Gladwell, G. & Zhu, H. (2002), ‘Courant’s nodal line theorem and its discrete counterparts’, *The Quarterly Journal of Mechanics and Applied Mathematics* **55**, 1–15.
- Hall, K. (1970), ‘An r-dimensional quadratic placement algorithm’, *Management Science* **17**, 219–229.
- Ham, J., Lee, D., Mika, S. & Schölkopf, B. (2004), A kernel view of the dimensionality reduction of manifolds, in ‘Proceedings of the Twenty-first International Conference on Machine Learning’, p. 47.
- Ham, J., Lee, D. & Saul, L. (2005), Semisupervised alignment of manifolds, in ‘Proceedings of the Annual Conference on Uncertainty in Artificial Intelligence’, Vol. 10, pp. 120–127.
- Hammond, D., Vandergheynst, P. & Gribonval, R. (2011), ‘Wavelets on graphs via spectral graph theory’, *Applied and Computational Harmonic Analysis* **30**, 129–150.
- Han, X., Jovicich, J., Salat, D., van der Kouwe, A., Quinn, B., Czanner, S., Busa, E., Pacheco, J., Albert, M., Killiany, R. et al. (2006), ‘Reliability of MRI-derived measurements of human cerebral cortical thickness: The effects of field strength, scanner upgrade and manufacturer’, *NeuroImage* **32**, 180–194.
- Holzrichter, M. & Oliveira, S. (1999), ‘A graph based method for generating the Fiedler vector of irregular problems’, *Parallel and Distributed Processing, Lecture Notes in Computer Science (LNCS)* **1586**, 978–985.
- Huang, S.-G., Lyu, I., Qiu, A. & Chung, M. (2020), ‘Fast polynomial approximation of heat kernel convolution on manifolds and its application to brain sulcal and gyral graph pattern analysis’, *IEEE Transactions on Medical Imaging* **39**, 2201–2212.
- Jones, S., Buchbinder, B. & Aharon, I. (2000), ‘Three-dimensional mapping of cortical thickness using Laplace’s equation’, *Human Brain Mapping* **11**, 12–32.
- Joshi, A., Shattuck, D. W., Thompson, P. M. & Leahy, R. M. (2009), ‘A parameterization-based numerical method for isotropic and anisotropic diffusion smoothing on non-flat surfaces’, *IEEE Transactions on Image Processing* **18**, 1358–1365.
- Kim, W., Pachauri, D., Hatt, C., Chung, M., Johnson, S. & Singh, V. (2012), Wavelet based multi-scale shape features on arbitrary surfaces for cortical thickness discrimination, in ‘Advances in Neural Information Processing Systems’, pp. 1250–1258.
- Kirby, M. (2000), *Geometric Data Analysis: An empirical approach to dimensionality reduction and the study of patterns*, John Wiley & Sons, Inc. New York, NY, USA.
- Koren, Y. & Harel, D. (2002), ‘A multi-scale algorithm for the linear arrangement problem’, **2573**, 296–309.
- Korfiatis, P., Kalogeropoulou, C., Karahaliou, A., Kazantzi, A. & Costaridou, L. (2011), ‘Vessel tree segmentation in presence of interstitial lung disease

- in MDCT', *IEEE Transactions on Information Technology in Biomedicine* **15**, 214–220.
- Lehoucq, R. & Sorensen, D. (1996), 'Deflation techniques for an implicitly restarted arnoldi iteration', *SIAM Journal on Matrix Analysis and Applications* **17**, 789–821.
- Lévy, B. (2006), Laplace-Beltrami eigenfunctions towards an algorithm that “understands” geometry, in 'IEEE International Conference on Shape Modeling and Applications', p. 13.
- Lindvere, L., Janik, R., Dorr, A., Chartash, D., Sahota, B., Sled, J. & Stefanovic, B. (2013), 'Cerebral microvascular network geometry changes in response to functional stimulation', *NeuroImage* **71**, 248–259.
- Mahadevan, S. & Maggioni, M. (2006), 'Value function approximation with diffusion wavelets and laplacian eigenfunctions', *Advances in Neural Information Processing Systems* **18**, 843.
- Malladi, R. & Ravve, I. (2002), Fast difference schemes for edge enhancing Beltrami flow, in 'Proceedings of Computer Vision-ECCV, Lecture Notes in Computer Science (LNCS)', Vol. 2350, pp. 343–357.
- Nain, D., Styner, M., Niethammer, M., Levitt, J., Shenton, M., Gerig, G., Bobick, A. & Tannenbaum, A. (2007), Statistical shape analysis of brain structures using spherical wavelets, in 'IEEE Symposium on Biomedical Imaging ISBI', Vol. 4, pp. 209–212.
- Nilsson, J., Sha, F. & Jordan, M. (2007), Regression on manifolds using kernel dimension reduction, in 'Proceedings of the 24th international conference on Machine learning', ACM, pp. 697–704.
- Perona, P. & Malik, J. (1990), 'Scale-space and edge detection using anisotropic diffusion', *IEEE Trans. Pattern Analysis and Machine Intelligence* **12**, 629–639.
- S., F. & H., M. (2008), 'Non-parametric regression between manifolds', *Advances in Neural Information Processing Systems* **21**, 1561–1568.
- Schölkopf, B. & Smola, A. J. (2002), *Learning with Kernels: Support Vector Machines, Regularization, Optimization, and Beyond*, MIT Press.
- Shang, Y., Deklerck, R., Nyssen, E., Markova, A., de Mey, J., Yang, X. & Sun, K. (2011), 'Vascular active contour for vessel tree segmentation', *IEEE Transactions on Biomedical Engineering* **58**, 1023–1032.
- Shawe-Taylor, J. & Cristianini, N. (2004), *Kernel methods for pattern analysis*, Cambridge University Press.
- Sochen, N., Kimmel, R. & Malladi, R. (1998), 'A general framework for low level vision', *IEEE Transactions on Image Processing* **7**, 310–318.
- Sun, J., Ovsjanikov, M. & Guibas, L. J. (2009), 'A concise and provably informative multi-scale signature based on heat diffusion.', *Comput. Graph. Forum* **28**, 1383–1392.
- Tang, B., Sapiro, G. & Caselles, V. (1999), Direction diffusion, in 'The Proceedings of the Seventh IEEE International Conference on Computer Vision', pp. 2:1245–1252.
- Taubin, G. (2000), Geometric signal processing on polygonal meshes, in 'EUROGRAPHICS', Eurographics Association.

- Trusty, T. (2007), 'A relation between the multiplicity of the second eigenvalue of a graph Laplacian, Courant's nodal line theorem and the substantial dimension of tight polyhedral surfaces', *Electron Journal of Linear Algebra* **16**, 315–24.
- Wang, Y., Ombao, H. & Chung, M. (2018), 'Topological data analysis of single-trial electroencephalographic signals', *Annals of Applied Statistics* **12**, 1506–1534.
- Wu, G., Wang, Q., Lian, J. & Shen, D. (2013), 'Estimating the 4d respiratory lung motion by spatiotemporal registration and super-resolution image reconstruction', *Medical physics* **40**(3), 031710.
- Yger, F. & Rakotomamonjy, A. (2011), 'Wavelet kernel learning', *Pattern Recognition* **44**(10-11), 2614–2629.